Fault controls spatial variation of fracture density and rock mass strength within the Yarlung Tsangpo Fault damage zone (southern Tibet)

Xueliang Wang[a,b,c*], Giovanni Battista Crosta[d*], John J. Clague[e], Douglas Stead[e], Juanjuan Sun[a,b,c], Shengwen Qi[a,b,c], Haiyang Liu[a,b,c]

[a] Key Laboratory of Shale Gas and Geoengineering, Institute of Geology and Geophysics, Chinese Academy of Sciences, Beijing 100029, China
[b] Institutions of Earth Science, Chinese Academy of Sciences, Beijing 100029, China
[c] University of Chinese Academy of Sciences, Beijing 100049, China
[d] Department of Earth and Environmental Sciences, University of Milano-Bicocca, Milan 20126, Italy
[e] Department of Earth Sciences, Simon Fraser University, Burnaby, BC V5A 1S6, Canada

Abstract: The extent of the fault damage zone remains an outstanding challenge confounding attempts to assess rock mass physical and mechanical properties, the effects on landscape evolution and slope stability, and to delineate safe places for human occupation and infrastructure development. Quantifying the relationship between faulting and the spatial geometrical and mechanical characteristics of a rock mass controlled by faulting is difficult, mainly because of varying lithology and rock mass characteristics, the effects of topography and vegetation and local erosion of weaker rock mass. Recent technological developments including Unmanned Aerial Vehicles, terrestrial laser scanning, photogrammetry and point cloud analysis software tools greatly enhance our ability to investigate the issues using the Yarlung Tsangpo (YLTP) Fault of southern Tibet as a case study where ideal geological conditions exist to investigate the relationship. In this study, the procedures, investigation approaches, evidence and criteria for defining the threshold distance for damage zones of YLTP Fault of southern Tibet were studied quantitatively by combining the spatial variations of fracture density, rock mass strength, rockfall inventory and previous thermal evidence. The results have been compared with published data from the evidence of thermal effects related to the exactly the same fault and show a good match between internal thermal action and rock mass physical and mechanical properties controlled by the same faulting. The extent of threshold distance of damage zone of the YLTP Fault is estimated as 5.9±0.6km. Within the damage zone, fracture density and cohesion of the rock mass show power curve relations with distance from the YLTP Fault. The internal dynamic action of fault controls rock mass physical and mechanical properties in the study area. The fault first affects the characteristics of rock mass structures, and then the orientation of the rock structures influences the stability of slope leading to rockfall.

Keywords: Fault damage zone, rock mass strength, fracture density, rockfall, southern Tibet.

1. Introduction

Faults and fault materials are a major controlling factor for superficial and shallow processes such as slope stability, groundwater flow and surface hydrology, underground excavations, hydrocarbons extraction and storage, and mining (De Joussineau & Aydin,2007; Bense et al., 2013; Laubach et al., 2014). Localized deformations at low confining stresses cause the formation of zones characterized by heterogeneous and anisotropic properties (Frankel et al., 2007; Gudmundsson, 2011). As a consequence, landslide susceptibility assessment (Dai et al., 2002: Wang et al., 2014), groundwater flow modeling (Faulkner et al., 2010; Bense et al., 2013) and design of superficial and underground structures (Aydin et al., 2004), require a detailed description of the zones affected by faulting (Faulkner et al., 2010). Fault core and damage zone are definitions which embrace the entire rock mass volume

around a fault “plane” (Faulkner et al., 2010; Laubach et al., 2014). Such a volume can be affected by a more or less important deterioration due to the stress and displacement concentration. The fault core is the zone where most of the displacements are accommodated. The damage zone is the portion of rock mass characterized by secondary structures including mainly fractures, secondary faults and zones with more abundant micro-fracturing, porosity and groundwater flow. In landslide susceptibility mapping, the distance from fault core has been frequently used as an index to quantify the potential triggering of fault-related landslide (Wang et al.,2014). However, spatial differences in fault-controlled geometrical characteristics (e.g. fracture density) and the effects of faulting on the mechanical properties of rock (e.g. rock mass strength) are typically defined empirically or at a mesoscale with limited field evidence (Faulkner et al., 2010; Mizoguchi and Ueta, 2013; Laubach et al., 2014), limiting their value. Consequently, we suggest this distance should be the main focus in the geological characterization of fault damage and its engineering importance.

In the geomorphological literature, it has been recognized that the geometrical and mechanical characteristics of a rock mass are both important in controlling relief and stability of slope (Burbank et al., 1996; Crosta et al., 2014; DiBiase et al., 2018; Wang et al., 2020). However, the fault-controlled spatial variation of geometrical characteristics (i.e. fracture density) and a quantitative description of the effects of faulting on the mechanical properties of the rocks within a specific threshold area have rarely been quantified (Caine et al., 1996; Faulkner et al., 2010; Laubach et al., 2014). Such quantification is often hampered by certain conditions mainly including: (1) large faults could result in varying rock mass characteristics within a specific area; (2) changes in lithology along and around the fault could render it difficult to have comparable conditions; (3) the effects of topography and vegetation obscuring damaged rock mass outcrops, limiting their number, size and distribution and then the possibility to build a robust data set; (4) the local erosion of sections of weaker rock mass. At the same time, some of the above listed features can support the characterization and analysis of these damaged zones, as by back analysis of landslides in areas with different landslide types and abundance. The availability of high-resolution topographic data (i.e. laser scanner and photogrammetric point clouds) can be of help at studying both small and large features supporting the description of the degree of fracturing at different spatial scales (Oskin et al., 2007).

As a consequence, in order to assess the landslide susceptibility of the rock mass strength for construction, it is important to define some basic rules for the identification, mapping, sampling and testing of the extent of these zones and the properties of the involved materials (e.g. breccias, cataclasite, mylonite). The total thickness of the fault zone will depend on the size of the fault, the total amount of cumulated displacement, the type of fault, the overburden depth for the considered zone of the fault, the affected lithology. Many of the same factors will also controls the physical, chemical and mechanical characteristics of the fault materials (Laubach et al., 2014). Using recent technologies including Unmanned Aerial Vehicle (UAV), terrestrial laser scanning, and photogrammetry and point cloud analysis software tools (e.g. AgiSoft, Photoscan and Coltop; Jaboyedoff et al.,2007), we attempted to determine the best procedures, investigation approaches, evidence and criteria for defining the threshold distance for damage zones around faults. Combining geometrical, mechanical characteristics and published thermal evidence (Quidelleur et al., 1997), quantitative description of the effects of faulting on rock mass physical and mechanical properties were quantified to reveal the dynamic action of fault.

2. Study area

In this study, we selected Wolong (WL) region, an area of Tibet where ideal geological conditions exist, to investigate the relationship between faulting and the spatial geometrical and mechanical characteristics of a rock mass controlled by faulting (Fig. 1). In the WL region, Yarlung Tsangpo (YLZP) River turns abruptly to the northwest, providing excellent exposures of structures and rocks along the YLZP Fault. The area is affected by the YLZP Fault that belongs to a south-dipping thrust system composed of at least five south dipping thrust faults (Heim & Gansser, 1939; Yin et al., 1999; Murphy & Yin, 2003). YLZP suture zone between the Indian and the

Eurasian plates has been reactivated by northward back thrusting and dextral strike-slip movement (Burg & Chen, 1984) with an underthrusting rate of 21.3 mm/yr of the Indian Shield (Murphy & Yin, 2003) and a right-lateral slip rate of 2.6±0.7 mm/yr (Chen et al., 2004). The nearly E–W trending suture zone extends for more than 2000 km in southern Tibet, whose deformation along the multiple fault planes of suture zone is complex and shows variations from place to place, depending mainly on its orientation (Aitchison et al., 2011; Yin et al., 1994; Xu et al., 2015). For the geological description of the area we relied on Quidelleur et al. (1997), Chen et al. (2004) and Xu et al. (2015). The lithology of the area is mainly diorite and granite with a small component of gneiss.

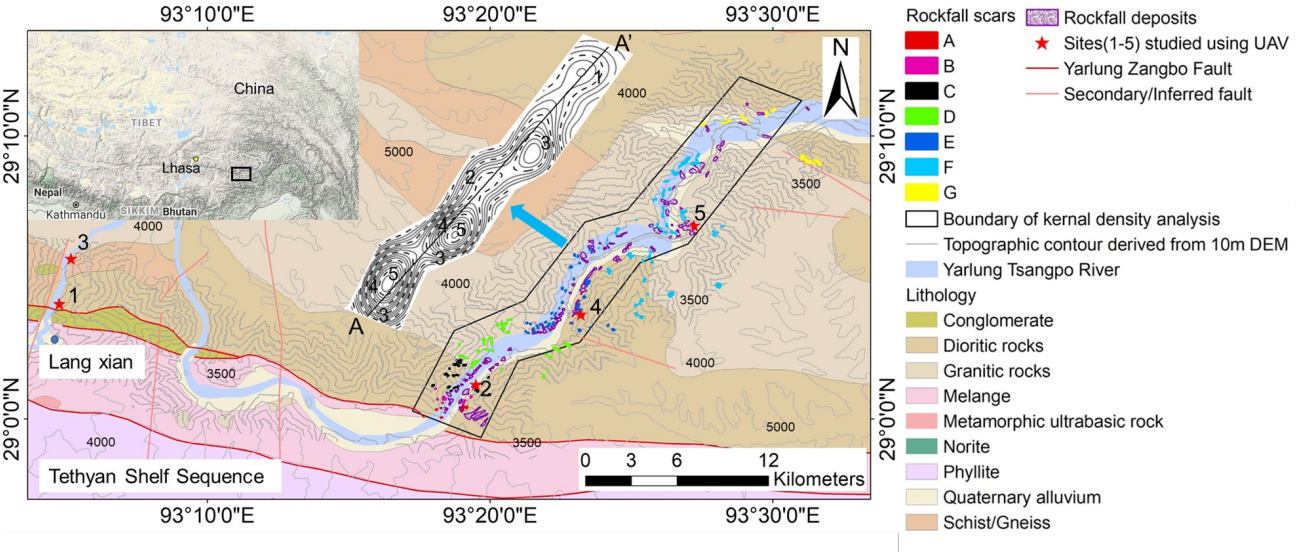

Fig.1 Location of the five surveying sites (1 to 5) and 407 rockfalls, including 284 rockfalls scars and 123 rockfalls deposits, with respect to the YLTP Fault core. Rockfall scars are zoned in 7 main clusters for back analysis of rock mass strength (Fig. 7), A to G, considering similar geometrical characteristics of the rock slopes and rock mass. Our 30-km measurement area covered by UAV at five sites and 10-m DEM for rockfalls identification on the whole slopes traverse along the YLZP river valley. Rockfall iso-density contours obtained through bivariate kernel density estimation by ArcGIS are shown.

3. Methodology

Both the geometrical characteristics of rock mass structures and rock mass strength could be controlled by a fault within a certain area (Osmundsen et al., 2009). The results of geometrical characteristics of rock mass structures and rock mass strength within the same fault zone should be consistent approximately if the approaches are used suitably. Hence, we firstly explored the spatial variation in the geometrical characteristics of the rock mass structures. Rock mass structures at the slope scale were identified and measured using a UAV at five selected sites at varied distances from the YLTP Fault core (Fig. 1), with the consideration that exhumation doesn't influence fracture measurements at the surface (Savage & Brodsky, 2011). The selection of the sites was based on the outcrop rock mass conditions and the rock mass structures present. The horizontal distances of the five sites from the YLZP Fault core are 0.5 km, 3.0 km, 3.4 km, 8.5 km and 13.5 km (Fig. 1). To get precise geometrical data of rock mass structures, we set at least six ground control points (GCP) at each site when flying UAV. The UAV used in our study is Phantom 4 RTK that provides real-time, centimeter-level positioning data for improved absolute accuracy on image metadata (https://www.dji.com/ca/ phantom-4-rtk). To satisfy the requirement of data resolution, we ensured lateral overlap ratio of aerial photography by UAV more than 65% and heading overlap ratio more than 75%. We sub-sampled point clouds to a minimum point spacing of 0.1 m by Agisoft Photoscan (AgiSoft LLC, 2010).

At each site, the same window (100 x 100 x 100 m) was selected for measuring the dip/dip direction and spacing

of all visible rock mass joints structures by PhotoScan, Coltop (Jaboyedoff et al.,2007) (Figs. 4a and b) and ESRI ArcMap 10 software. We generated the stereographic projections by inputting the data into Rocscience DIPS 7.0 software. We selected different appropriate viewpoints in point cloud model of PhotoScan to generate orthographic projection images according to the occurrence of each joint, and then the image data with scale were imported into ArcMap. By ArcMap, we vectorized each joint and measured discontinuity spacing in detail. The joint size measured is based on the quantity of data obtained by UAV, with a minimum joint spacing of 0.3m (Fig. 4b).

Fracture density is an important parameter in quantifying the geometrical character of the rock mass (Faulkner et al., 2010). To estimate fracture density, we used three-dimensional geomechanical data to provide a joint volume count (Jv), which we then took as a measure of block size and of the total number of joints encountered in a cubic meter of the fractured rock mass (Palmstrom, 2005). After measuring the spacing of the joints, we calculated mean value of each group of joints. Using the mean spacing values of the joint sets, we calculated Jv as follows (Palmstrom, 2005):

$$Jv=\frac{1}{S1}+\frac{1}{S2}+\frac{1}{S3}+\ldots+\frac{1}{Sn} \qquad (1)$$

where S_i is the mean joint spacing for each joint set, for i = 1, 2, . . ., n.

To verify the results of joint spacing and fracture density Jv at the five sites (1-5), we independently measured fallen block sizes using the UAV and Photoscan imagery (Fig. 2).

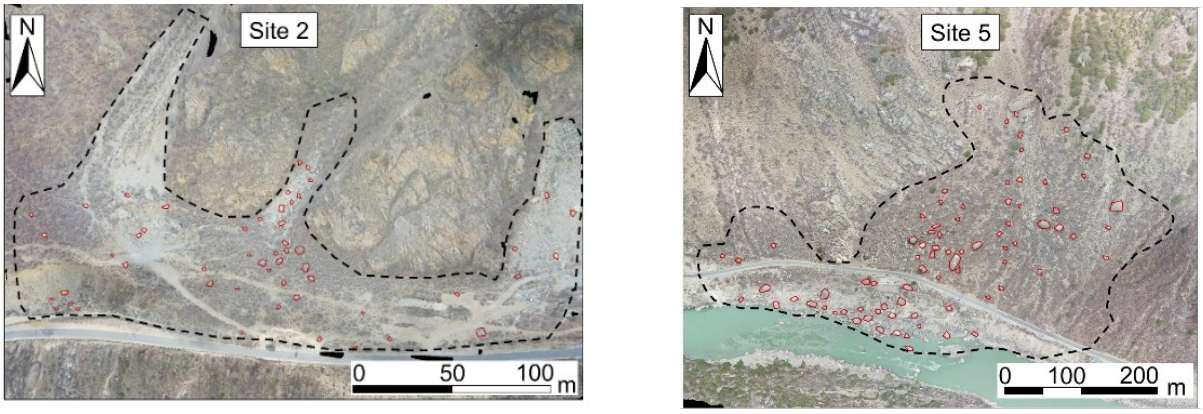

Fig. 2 Orthophotos of the foot of mountain areas used for grain size of fallen blocks analysis (samples of sites 2 and 5).

Rock mass strength is a very difficult characteristics to be defined in a large area because of lack of suitable approaches and its inherent geology uncertainty (Hoek, 1983; Gudmundsson, 2011). Some studies (Hoek, 1994; Schmidt & Montgomery,1995; Evans et al., 1997; Shipton et al., 2002; Crosta et al., 2014) have tried to solve the problem. Various authors tackled the subject from a geomorphological and geomechanical point of view. Schmidt & Montgomery (1995) proposed an approach to define rock mass strength by analyzing relief and slope angle based on back analysis. Crosta et al. (2014) adopted an advanced geomechanical modeling approach to characterize rock masses on Mars starting from the distribution of landslides. Based on data of slope and relief of historical rockfall scars and reference to previous studies (Schmidt & Montgomery, 1995; Burbank et al., 1996; Montgomery & Brandon,2002; Crosta et al., 2014; DiBiase et al,2018), the rock mass strength of bedrock was back-calculated by the Culmann method under the precondition that bedrock relief is controlled by rock strength in the study area. When the present relief of bedrock areas is larger than the limit relief, the bedrock is prone to generate rockfalls.

Using data from helicopter-based remote sensing imagery and a DEM of 10 m resolution of the complete study

area, a total of 407 historical rockfalls inventory including 284 rockfalls scars on bedrocks (Fig.1 and Fig.3) and 123 rockfalls deposits at toe of slopes were identified (Fig. 1). 284 rockfall scars were identified based on the fresh bedrock color left on the scars (Fig.4). 123 rockfalls deposits at the foot of slopes were identified based on the shape of deposit (e.g. pyramid) and identifiable rockfall blocks (e.g. meters) left on the deposits (Fig.4). Because 284 rockfalls scars were identified on bedrocks with steep slope, it is not easy or even impossible to track their deposits. However, from the viewpoint of statistics rather than for a specific rockfall concerned, we combined the 284 rockfalls scars on bedrocks and 123 rockfalls deposits together to interpolate the rockfall density map. By the calculation of kernel density tool in ArcMap, we interpolated the rockfall density map in a search radius of 2.5 km considering the conditions of width of valley and slopes on site and rockfall size (Fig.1). By ArcMap, we extracted the value of rockfall density along the A-A profile in Fig.1, and created the value of rockfall density vs distance from fault core in Fig.8.

We measured the relief at scar sites which were considered as limit relief thresholds by ArcMap. We first extracted the maximum and minimum elevation of rockfall scars by ArcMap. Then the limit relief rockfall scar was calculated by Eq. (2). Meanwhile, we calculated mean slope of the rockfall scar area by ArcMap. Lastly, we calculated limit relief H_i and hillslope gradient (β) of all rockfalls scars.

$$H_i = H_{imax} - H_{imin} \qquad (2)$$

where i is the number of rockfall scar, H_{imax} and H_{imin} are the maximum and minimum elevations of rockfall scar i.

The Culmann's two-dimensional slope stability model based on principles of limit-equilibrium was used to back-calculate the rock mass strength at the landscape scale, which predicts a bounding relationship between hillslope gradient (β) and relief such that the maximum hillslope height (H_c) is given by (Culmann, 1875).

$$H_c = \frac{4C}{\rho g} \frac{sin\beta cos\varphi}{[1-\cos(\beta-\varphi)]} \qquad (3)$$

where c is cohesion, and φ is the internal friction angle.

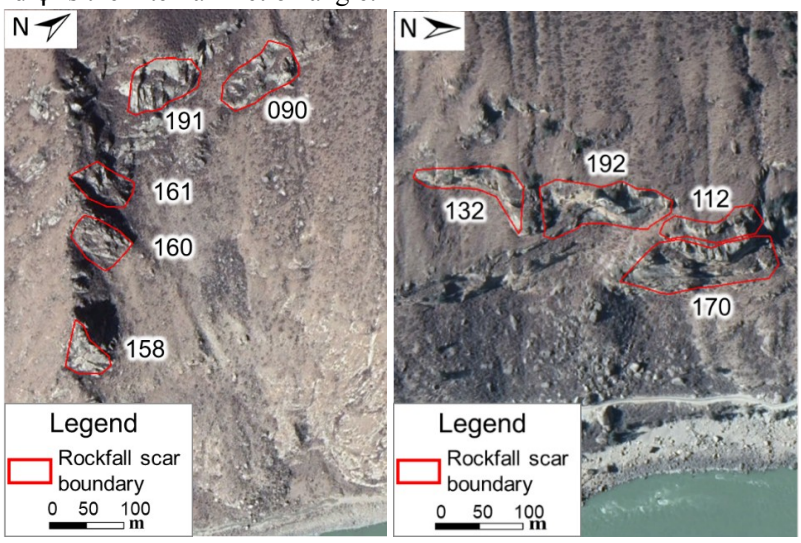

Fig. 3 Samples of oblique air photographs of rockfall scars (Fig.1) analyzed in Wolong region

4. Results

The types of rock mass structures controlling the stability of slopes include primary rock fabric (e.g. sedimentary stratification and metamorphic foliation), and secondary tectonic and weathering structures (Stead and

Wolter, 2015). The dominant structural type in the diorite and granite rock mass in the WL region is tectonic (Townend et al., 2004). Overall a total of 2322 structures were measured including 537, 510, 560, 417 and 298 structures at sites 1 to 5 respectively (Fig. 4). Based on the results, 5 predominant joint sets were identified in the study area. Joint sets J1 and J2, whose dips are greater than 56°, are conjugate joint sets created probably due to tectonism under a condition of vertical maximum principal stress. The two joint sets are most commonly and clearly exposed in the areas between sites 1 to 4. At site 5 and areas beyond that, joint sets J1 and J2 are few, with J1 absent in some places. Joint set J3 appears to represent unloading/stress-relief structures that parallel the slope surface and are exposed between sites 1 to 5. The dip of joint set J4 mainly exposed at sites 1 to 5 is less than 41°. Joint set J4 also represents unloading structures created during denudation of the diorites and granite. Joint set J5 whose mean dip is about 40° is mainly found at site 5 and areas beyond site 5. It should be noted that the dip/dip direction of the joint sets at the first four sites have very similar characteristics. In contrast, the dip/dip direction of the joints recorded at site 5 show significantly different characteristics including the disappearance of joint set, J1, and the appearance of joint set, J5 (Fig. 3 and Fig. 8).

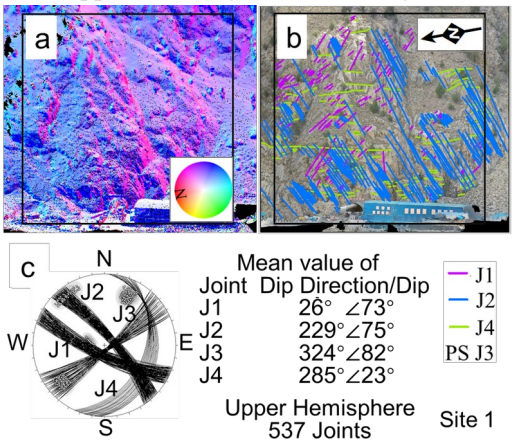

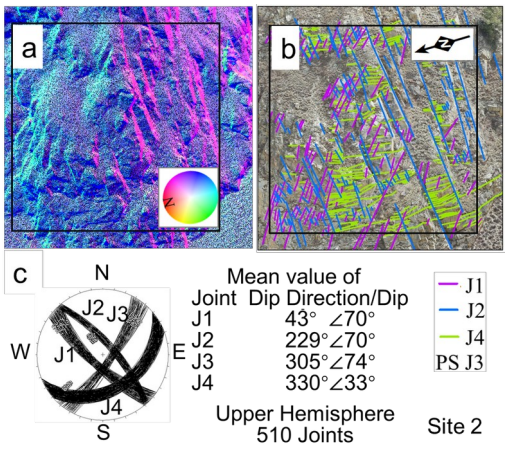

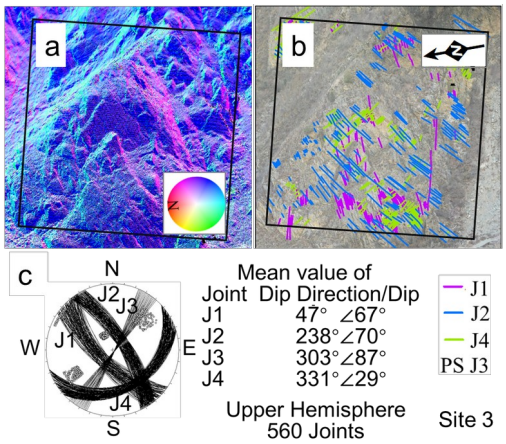

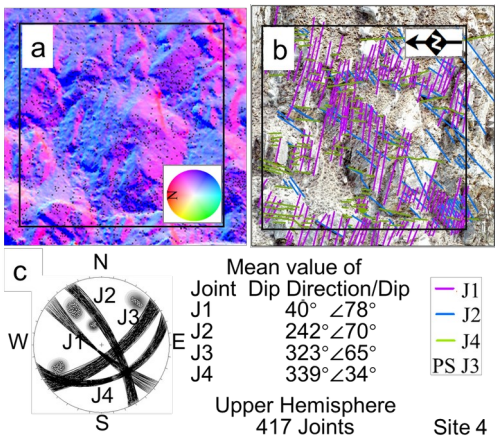

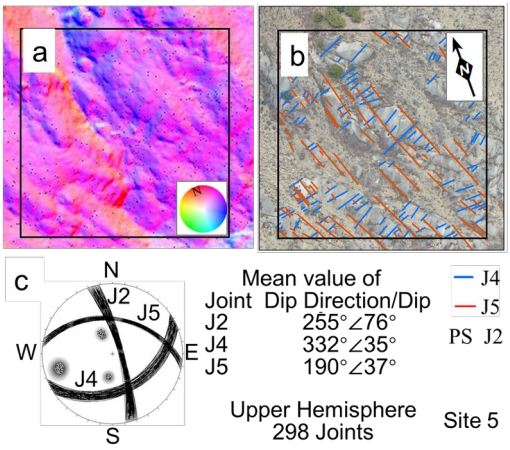

Fig. 4 Coltop images (a) in colours representing the local orientation of five joint sets (b) at five sites (Fig. 1 and Fig. 3) and stereographic projections (c). At each site, a window of 100 x 100 x 100 m was selected for measuring the dip/dip direction (c) and spacing of all visible rock mass joints.

The J1 to J5 joint set spacing and their mean values at each site was measured as shown in Fig. 5 and Table 1. Influenced by tectonics, the relationship between mean spacing of joint sets with distance from the fault core show a strong positive power relationship (Fig. 6). The rock mass exposed at site 3 in contrast to the other four sites is predominantly gneiss (Fig. 1). The rock strength of the gneiss measured on site by Schmidt hammer testing (Aydin & Basu 2005) is lower than that of diorite and granite. As observed at site 3, the spacing of the joint sets within gneiss is smaller relative to the same joint sets in the diorite under the similar condition of tectonism (Fig. 5). For consistency here we only considered the spacing of the joint sets within the same diorite lithology in building the relationship. The joint volumetric count, Jv, at varying distance (d) from the fault core is calculated using the joint set spacing (Table 1) and shows a strong negative power relationship (Fig. 6) albeit with relatively large variability at site 1. There is also a marked exponential relation between the mean size of fallen blocks and distance from the fault core (Fig. 5 and Fig. 6). This indicated that the sizes of the rockfall blocks and the joint set spacing agree well even when they are obtained by different methods.

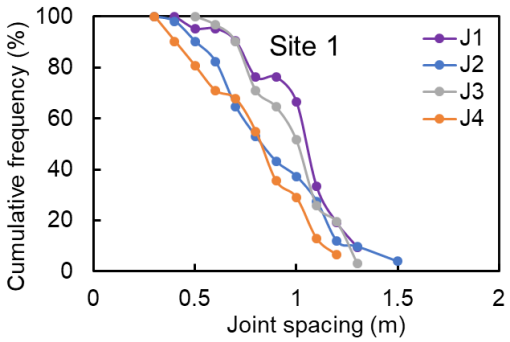

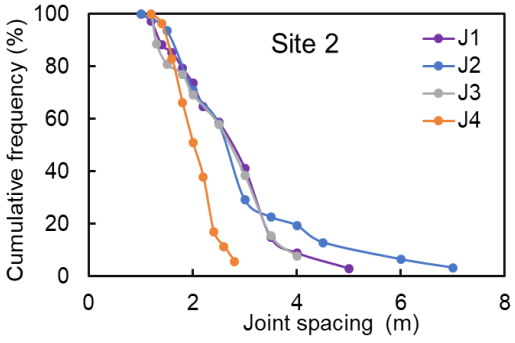

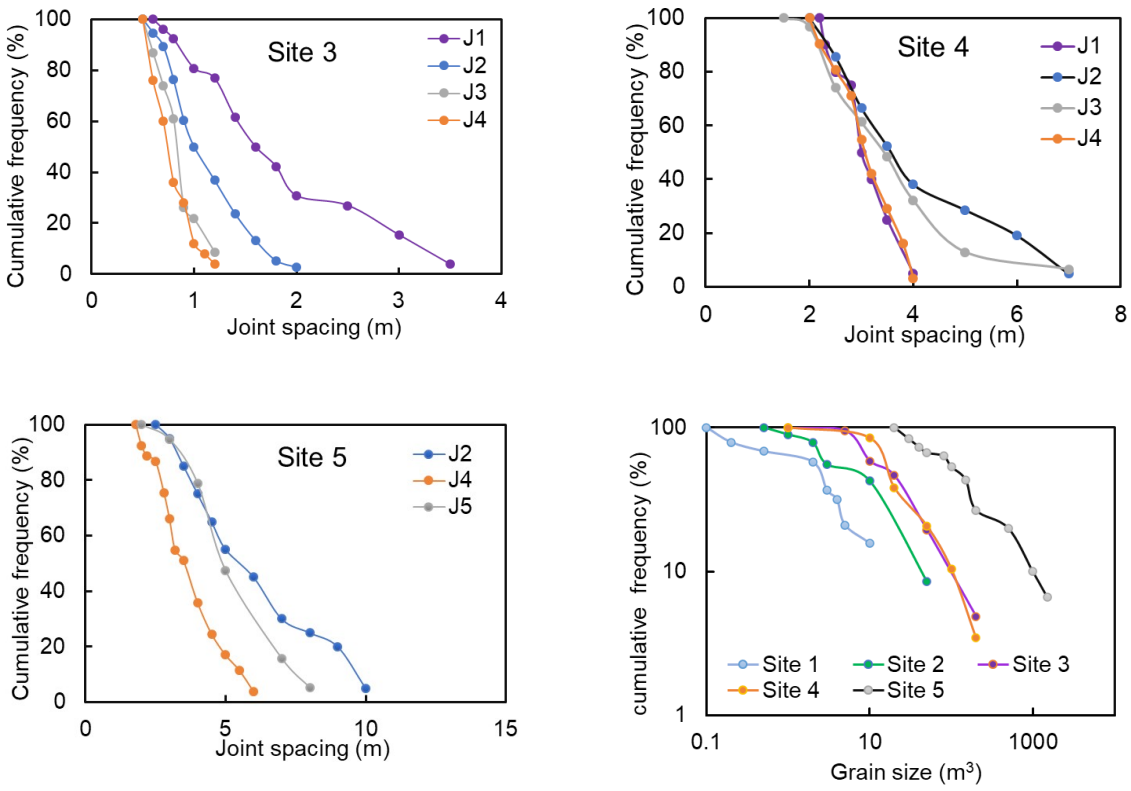

Fig. 5 Cumulative frequency of all joints spacings at each site (site 1 to 5) and cumulative grain size of fallen blocks distributions from field surveys at each site (site 1 to 5)

Table 1 Mean spacing of joints at each site (1 to 5)

Joint number at each site	Horizontal distance from fault core (km)	Mean value of joint spacing (m)	Variable of coefficient
	Site 1		
J1	0.50	0.92	0.26
J2	0.50	0.79	0.41
J3	0.50	0.89	0.24
J4	0.50	0.71	0.39
	Site 2		
J1	3.00	2.26	0.35
J2	3.00	2.37	0.54
J3	3.00	2.25	0.36
J4	3.00	1.90	0.34
	Site 3		
J1	3.40	1.56	0.45
J2	3.40	1.03	0.35
J3	3.40	0.74	0.27
J4	3.40	0.67	0.31
	Site 4		
J1	8.50	2.84	0.16
J2	8.50	3.43	0.41

J3	8.50	3.05	0.42
J4	8.50	2.84	0.21
	Site 5		
J2	13.50	5.30	0.42
J4	13.50	3.30	0.32
J5	13.50	3.90	0.37

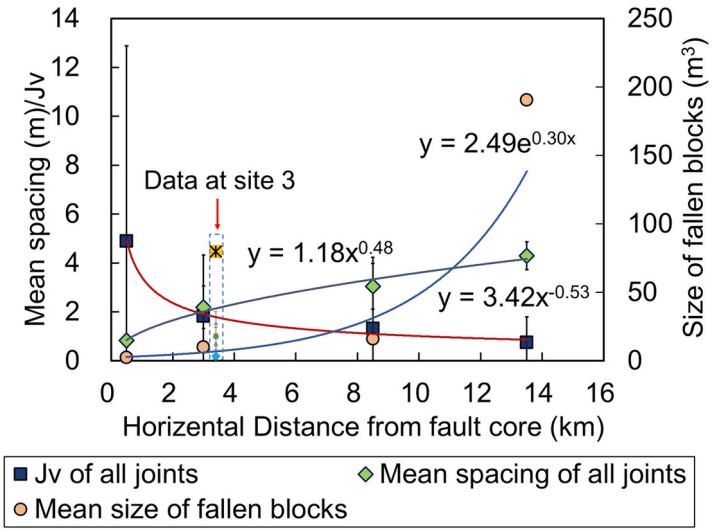

Fig. 6 Logarithmic and exponential relationships between mean spacing, computed Jv fracture density and the size of fallen blocks as a function of distance from the fault core.

Using the Culmann method, we back-calculate bedrock mass strength based on measurements of slope and relief of total 284 rockfall scars in the WL region (Fig. 7). Values of cohesion (c) show a significant increase with distance (d); they fit the power curve relation, c=208.64×d^0.12 (Fig. 8). In contrast, values of internal friction angle have a limited range (23-28°) and do not change significantly with distance from the fault core. Rock mass strength calculated by the Culmann method at distances up to 5.3 km from the fault core is less than 300 kPa (Fig. 8) and within the range of values estimated for hillslope-scale strength (Schmidt and Montgomery, 1995). We attribute the low values of rock mass strength to fault damage and use them to define a fault damage zone. At distances > 6.5 km from the fault core, rock mass strength significantly increases. Mean rockfall density calculated using the spatial distribution of 407 rockfalls including 284 rockfall scars and 123 rockfall deposits (Fig. 1) by the bivariate kernel density estimation tool in ArcGIS up to 6.5 km from the fault core is about three times that beyond this distance (Fig. 8). Hence, we combined the results of geometrical and mechanical analysis of rock mass characteristics to estimate that the width of the damage zone of the YLZP Fault is 5.9 ± 0.6 km (Fig. 8).

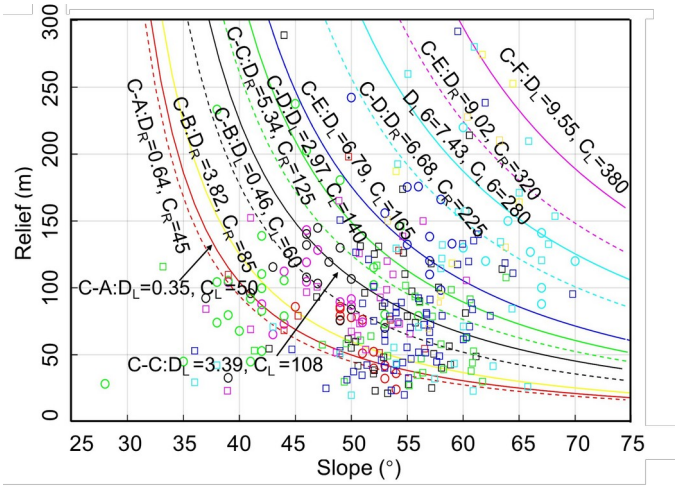

Fig. 7 Relief vs slope angle at 284 rockfall scars (see Fig. 1 for locations). Square and circle points represent data from left- (L)and right-hand (R) valley flanks. DL and DR (km) are the distances from fault core. CL and CR (kPa) are estimated cohesion values of bedrocks. C-A (to F) represent the 7 clusters (A to F) of rockfall scars in Fig. 1.

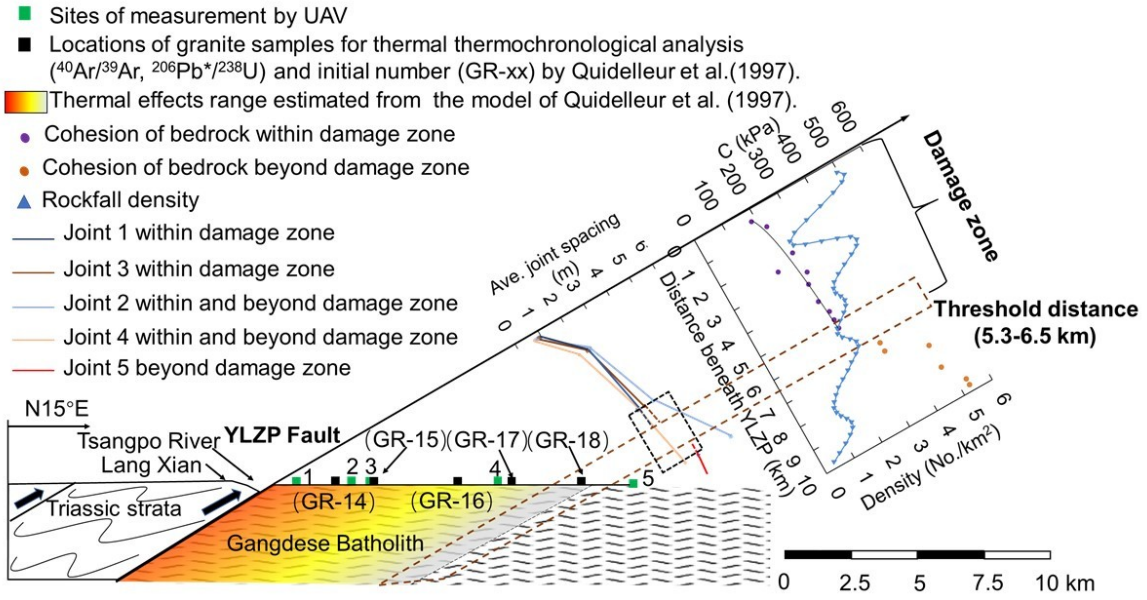

Fig. 8 Extent of the damage zone of the thrust plane of the YLZP Fault. Considering the divergency of 45° (Fig.1) and a constant 30° dip to the south for the fault (Quidelleur et al.,1997), the five sites (1 to 5) are situated between 0 and 6.8 km from the hanging wall of the YLZP Fault. The exposure and average spacing of joint sets with the distance from fault core, using 2322 joints (Fig. 2) measured by UAV at the five sites, are represented. Cohesion of bedrocks back calculated by means of the Culmann's approach on the whole slopes (Fig. 4b) and the rockfall density extracted from Fig. 1 along the A-A' profile vs distance from fault core are represented in the plots.

5. Discussion

We examined quantitatively the geometrical and mechanical characteristics of rock mass structures along the YLTP Fault, and infer that fault-induced deformation is the dominant control on rock mass strength within a fault damage zone that was estimated as 5.9 ± 0.6 km (Fig. 8). Quidelleur et al. (1997) studied the internal thermal properties and evolution of YLTP Fault using biotite and K-feldspar ages and numerical simulation in the WL region. We observe a good match between our threshold distance of damage along the YLTP Fault and the location of the boundary in their thermal model (Fig. 8). Previous studies indicated a trend of increasing damage zone width with displacement of fault, and that a lack of data for large faults (with displacements larger than 100 m) limits the

possibility to find a statistically valid relationship for larger faults (Savage & Brodsky, 2011, De Joussineau & Aydin, 2007; Faulkner et al., 2010; Laubach et al., 2014; Torabi et al.,2019). By combining the displacement data of Quidelleur et al. (1997) and our damage zone width estimate, we offer value of 5.9 ± 0.6 km close to the maximum reported in the literature (Fig. 9). Within this damage zone, both fracture density and rock mass cohesion exhibit a power law relation with distance from the core of the YLZP Fault.

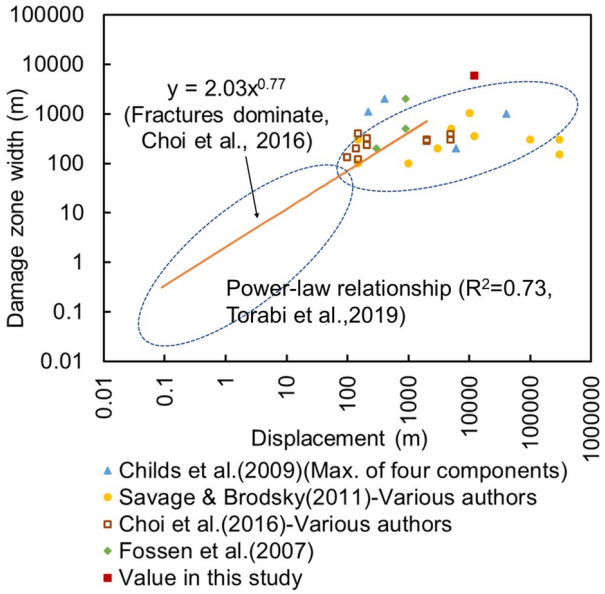

Fig. 9 Log–log plots of damage zone width against displacement of large faults (> 100 m displacement, Torabi et al., 2019) from the previous studies and our study on YLZP fault.

We observe an inverse relationship between mean slope angle and topographic relief in our study area (Fig. 7), consistent with the results of Schmidt and Montgomery (1995), Frattini & Crosta (2013), Crosta et al. (2014), and DiBiase et al. (2018). Hence, we infer that rock mass strength is an important factor controlling relief in the area. However, Gabet et al. (2004) came to a different conclusion, suggesting that annual rainfall, not rock mass strength, is the controlling factor on relief in the Himalayas of central Nepal, leading to the result that mean hillslope angles decrease with increasing mean annual rainfall. In our whole study area, local annual precipitation is uniform. This difference possibly is due to different geological settings, climate conditions, and scales of the studies. In our study area, intense tectonic activity within major fault zones has affected the geometrical and mechanical characteristics of rock mass. Research on differences in rock mass strength related to different scales and different geological settings (e.g. tectonically active sites) is a worthwhile future endeavor.

Previous studies (Khazai & Sitar,2004; Huang & Li, 2009; Qi et al,.2010; Wang et al., 2020) have noted that faults have an important influence on triggering landslides and rockfalls; some of these researchers also discussed the relationships between number of landslides and distance from a fault. However, the process of faults controlling regional landslides and rockfall still suffers from a lack of quantitative description. We quantitatively show that spatial variation of the rock mass strength shows different trend within and beyond the threshold distance due to the shift of geometrical characteristics of rock mass structures controlled by the YLZP Fault (Fig. 8). Correspondingly, the density of rockfalls shows a significant shift at the threshold distance.

6. Conclusion

The extent of threshold distance of damage zone of the YLTP Fault is estimated as 5.9±0.6 km, which reaches values close to the maximum reported in literatures. Within the threshold distance of YLTP Fault, both fracture spacing and density (joint volumetric count) and rock mass cohesion exhibit a power law relation with distance

from the core of the YLZP Fault. Based on this relationship, we conclude that rock mass structure generated by internal dynamic action of faults is the dominant control on rock mass strength within the damage zone. To predict/ assess the influence of faults in controlling regional landslide and rockfall distribution, the spatial variation of the geometrical characteristics of jointing is a key issue for future investigations.

Acknowledgments This work was supported by the Second Tibetan Plateau Scientific Expedition and Research Program (STEP) (Grant No. 2019QZKK0904), the Strategic Priority Research Program of the Chinese Academy of Sciences (Grant No. XDA23090402), Application of Synthetic Aperture Radar-Based Geological Hazard Analysis Technology on the Strategic Electricity Transmission Passage of Sichuan-Tibet Plateau (Grant No. 52199918000C), Foundation of China Scholarship Council, and the CARIPLO 2016-0756 @RockHoRiZon - Advanced Tools for Rockfall Hazard and Risk Zonation at the Regional Scale project.

References

AgiSoft LLC. 2010. AgiSoft PhotoScan. http://www.agisoft.ru/products/photoscan/(date of access: 30 October 2010).

Aitchison, J.C., Xia, X., Baxter, A.T., Ali, J.R., 2011. Detrital zircon U–Pb ages along the Yarlung–Tsangpo suture zone, Tibet: implications for oblique convergence and collision between India and Asia. Gondwana Research. 20 (4), 691–709. https://doi.org/10.1016/j.gr.2011.04.002.

Aydin, A., Ozbek, A., Cobanoglu, I., 2004. Tunneling in difficult ground: a case study from Dranaz tunnel, Sinop, Turkey. Eng. Geol. 74(3-4), 293–301. https://doi.org/10.1016/j.enggeo.2004.04.003.

Aydin, A, Basu, A., 2005. The Schmidt hammer in rock material characterization. Eng. Geol. 81(1), 1-14. https://doi.org/10.1016/j.enggeo.2005.06.006

Bense, V.F., Gleeson, T., Loveless, S.E., Bour, O., Scibek, J., 2013. Fault zone hydrogeology. Earth Science Reviews. 127, 171-192, http://dx.doi.org/10.1016/j. earscirev.2013.09.008.

Burbank, D.W., Leland, J., Fielding, E., Anderson, R.S., Brozovic, N., Reid, M.R., Duncan, C.,1996. Bedrock incision, rock uplift and threshold hillslopes in the northwestern Himalayas. Nature. 379, 505-510. https://doi.org/10.1038/379505a0.

Burg, J.P., Chen, G.M., 1984. Tectonics and structural zonation of southern Tibet, China. Nature. 311, 219–223. https://doi.org/10.1038/311219a0.

Caine, J.S., Evans, J.P., Forster, C.B., 1996. Fault zone architecture and permeability structure. Geology. 24 (11), 1025-1028. https://doi.org/10.1130/ 0091-7613(1996)024<1025:FZAAPS>2.3.CO;2.

Chen Q., Freymueller J.T., Yang Z., Xu C.J., Jiang W.P., Wang Q., Liu J.N., 2004. Spatially variable extension in southern Tibet based on GPS measurements. Journal of Geophysical Research. 109, B09401. https://doi.org/10.1029/2002JB002350.

Childs, C., Manzocchi, T., Walsh, J.J., Bonson, C.G., Nicol, A., & Schopfer, M.P.J., 2009. A geometric model of fault zone and fault rock thickness variations. Journal of Structural Geology, 31, 117-127. https://doi.org/10.1016/j.jsg.2008.08. 009.

Choi, J. H., Edwards, P., Ko, K. and Kim, Y. S., 2016. Definition and classification of fault damage zones: a review and a new methodological approach: Earth-Science Reviews, 152, 70-87. https://doi.org/10.1016/j.earscirev.11.006.

Crosta, G.B., Utili, S., De Blasio, F.V., Castellanza R., 2014. Reassessing rock mass properties and slope instability triggering conditions in Valles Marineris, Mars. Earth and Planetary Science Letters. 388, 329–342, https://doi.org/10.1016/j.epsl.2013.11.053.

Culmann, C., 1875. Die Graphische Statik: Zurich, Switzerland, Meyer and Zeller, 644 p.

Dai, F.C., Lee, C.F., Ngai, Y.Y., 2002. Landslide risk assessment and management: an overview. Eng. Geol. 64(1):65–87. https://doi.org/10.1016/S0013-7952(01)00093-X.

De Joussineau, G., Aydin, A., 2007. The evolution of the damage zone with fault growth in sandstone and its multiscale characteristics. Journal of Geophysical Research. 112, B12401. https://doi.org/10.1029/2006jb004711.

DiBiase, R.A., Rossi, M.W., Neely, A.B., 2018. Fracture density and grain size controls on the relief structure of bedrock landscapes.

Geology. 46(5), 399-402. https://doi.org/10.1130/g40006.1.

Evans, J.P., Forster, C.B., Goddard, J.V., 1997. Permeability of fault-related rocks, and implications for hydraulic structure of fault zones. J. Struct. Geol. 19 (11), 1393-1404. http://dx.doi.org/10.1016/S0191-8141(97)00057-6.

Faulkner, D.R., Jackson, C.A.L., Lunnc, R.J., Schlische, R.W., Shipton, Z.K., Wibberley, C.A.J., Withjack, M.O., 2010. A review of recent developments concerning the structure, mechanics and fluid flow properties of fault zones. J. Struct. Geol. 32(11), 1557-1575. https://doi.org/10.1016/j.jsg.2010.06.009.

Fossen, H., Schultz, R.A., Shipton, Z.K., & Mair, K., 2007. Deformation bands in sandstone: a review. Journal of the Geological Society, 164, 1-15. https://doi.org/10.1144/0016-76492006-036.

Frankel, K. L., Dolan, J. F. Finkel, R. C. Owen, L. A. Hoeft, J. S., 2007. Spatial variations in slip rate along the Death Valley-Fish Lake Valley fault system determined from LiDAR topographic data and cosmogenic 10Be geochronology. Geophys. Res. Lett. 34, L18303, doi:10.1029/2007GL030549.

Frattini, P., Crosta, G.B., 2013. The role of material properties and landscape morphology on landslide size distributions. Earth and Planetary ScienceLetters. 361, 310-319. https://doi.org/10.1016/j.epsl.2012.10.029.

Gabet, E.J., Pratt-Sitaula, B.A., Burbank, D.W., 2004. Climatic controls on hillslope angle and relief in the Himalayas. Geology. 32(7), 629–632. https://doi.org/ 10.1130/g20641.1.

Gudmundsson, A., 2011. Rock fractures in geological processes. New York, Cambridge University Press. 18p.

Heim, A., Gansser, A., 1939. Central Himalaya, geological observations of the Swiss expeditions 1936. Memoires de la Socie´te´ Helvetiques des Sciences Naturelles, 73, 1–245.

Hoek E., 1983. Strength of jointed rock masses, Géotechnique, 33(3), 187–223.

Hoek E., 1994. Strength of rock and rock masses, ISRM News Journal, 2(2), 4–16.

Huang, R., & Li, W., 2009. Analysis of the geo-hazards triggered by the 12 May 2008 Wenchuan Earthquake, China. Bulletin of Engineering Geology and the Environment. 68, 363–371. https://doi.org/10.1007/s10064-009-0207-0.

International Society for Rock Mechanics (ISRM), 1978. Commission on standardization of laboratory and field tests, Suggested methods for the quantitative description of discontinuities in rock masses. Int. J. Rock Mech. Min. Sci. & Geomech. Abstr., 15(6), 319-368.

Jaboyedoff, M., Metzger, R., Oppikofer, T., Couture, R., Derron, M.H., Locat, J., Turmel, D., 2007. New insight techniques to analyze rock-slope relief using DEM and 3D-imaging cloud points: COLTOP 3D software. Proceedings of the 1st Canada-US rock mechanics Symposium, Vancouver, Canada. 27–31 May 2007, https://doi.org/10.1201/NOE0415444019.

Khazai, B., Sitar, N., 2004. Evaluation of factors controlling earthquake-induced landslides caused by Chi-Chi earthquake and comparison with the Northridge and Loma Prieta events. Eng. Geol., 71(1-2), 79–95. https://doi.org/10.1016 /s0013-7952(03)00127-3.

Laubach, S.E., Eichhubl, P., Hargrove, P., Ellis, M.A., Hooker, J.N., 2014. Fault core and damage zone fracture attributes vary along strike owing to interaction of fracture growth, quartz accumulation, and differing sandstone composition. J. Struct. Geol. 68 (part A), 207-226. https://doi.org/10.1016/j.jsg.2014.08.007.

Mizoguchi, K., Ueta, K., 2013. Microfractures within the fault damage zone record the history of fault activity. Geophys. Res. Lett. 40, 2023–2027, https://doi.org/10.1002/grl.50469

Montgomery, D.R., Brandon, M.T., 2002. Topographic controls on erosion rates in tectonically active mountain ranges. Earth and Planetary Science Letters. 201(3-4), 481–489. https://doi.org/10.1016/s0012-821x(02)00725-2.

Murphy, M.A., Yin, A., 2003. Structural evolution and sequence of thrusting in the Tethyan fold-thrust belt and Indus-Yalu suture zone, southwest Tibet. Geological Society of America Bulletin. 115(1), 21-34. https://doi.org/10.1130/0016-7606(2003)115<0021:SEASOT>2.0.CO;2

Oskin, M. E., Le, K. Strane, M. D., 2007. Quantifying fault-zone activity in arid environments with highresolution topography. Geophys. Res. Lett. 34, L23S05, https://doi.org/10.1029/2007GL031295

Osmundsen, P.T., Henderson, I., Lauknes, T.R., Larsen, Y., Redfield T.F., Dehls J., 2009. Active normal fault control on landscape and

rock-slope failure in northern Norway. Geology. 37(2), 135-138, https://doi.org/10.1130/g25208a.1.

Palmstrom, A., 2005. Measurements of and Correlations between Block Size and Rock Quality Designation (RQD). Tunnels and Underground Space Technology. 20(4), 362–377. https://doi.org/10.1016/j.tust. 2005.01.005

Qi S.W., Xu Q., Lan H.X., Zhang B. Liu J.Y., 2010. Spatial distribution analysis of landslides triggered by 2008.5.12 Wenchuan Earthquake. China. Eng. Geol. 116(1-2), 95-108. https://doi.org/10.1016/j.enggeo.2010.07.011.

Quidelleur X., Grove M., Lovera O.M., Harrison T. M., Yin A., Ryerson F.J., 1997. Thermal evolution and slip history of the Renbu Zedong Thrust, southeastern Tibet. Journal of Geophysical Research. 102(B2), 2659-2679. https://doi.org/10.1029/96JB02483.

Shipton, Z.K., Evans, J.P., Robeson, K.R., Forster, C.B., Snelgrove, S.S., 2002. Structural heterogeneity and permeability in faulted eolian sandstone: implications for subsurface modeling of faults. AAPG Bull. 86 (5), 863-883.

Savage H.M., Brodsky E.E., 2011. Collateral damage: Evolution with displacement of fracture distribution and secondary fault strands in fault damage zones. Journal of Geophysical Research. 116, B03405. https://doi.org/10.1029/2010JB007665.

Schmidt, K.M., Montgomery, D.R., 1995. Limits to relief. Science. 270 (5236), 617-620. https://doi.org/10.1126/science.270.5236.617.

Stead, D., Wolter, A., 2015. A critical review of rock slope failure mechanisms: The importance of structural geology. J. Struct. Geol. 74, 1-23. https://doi.org/10.1016/j.jsg.2015.02.002.

Torabi, A., Ellingsen, T.S.S., Johannessen, M.U., Alaei, B., Rotevatn, A. Chiarella, D., 2019. Fault zone architecture and its scaling laws: where does the damage zone start and stop? Geological Society, London, Special Publications. 496, https://doi.org/10.1144/SP496-2018-151.

Townend, J., M. D. Zoback, 2004, Regional tectonic stress near the San Andreas fault in central and southern California. Geophys. Res. Lett. 31, L15S11, https://doi.org/10.1029/2003GL018918.

Wang, X.L., Zhang, L.Q., Wang, S.J., Lari, S., 2014. Regional landslide susceptibility zoning with considering the aggregation of landslide points and the weights of factors. Landslides. 11, 399–409. https://doi.org/10.1007/s10346-013-0392-6.

Wang X.L., Frattini, P., Stead, D., Sun J.J., Liu H.Y., Valagussa A., Li L.H., 2020. Dynamic rockfall risk analysis. Eng. Geol. 272, 105622. https://doi.org/10.1016/j.enggeo.2020.105622.

Xu Z.Q, Dilek, Y., Yang, J.S., Liang, F.H., Liu, F., Ba, D.Z., Cai, Z.H., Li, G.W., Dong, H.W., Ji, S.C., 2015. Crustal structure of the Indus–Tsangpo suture zone and its ophiolites in southern Tibet. Gondwana Research. 27(2), 507-524. https://doi.org/10.1016/j.gr.2014.08.001.

Yin, A.,Harrison, T.M.,Ryerson, F.J.,Chen, W.,Kidd, W.S.F., Copeland, P., 1994. Tertiary structural evolution of the Gangdese thrust system, southeastern Tibet. Journal of Geophysical Research. 99(B9), 18175–18201. https://doi.org/ 10.1029/94JB00504.

Yin, A., Harrison, T.M., Murphy, M.A., Grove, M., Nie, S., Ryerson, F.J., Wang, X., Chen, Z., 1999. Tertiary deformation history in southeastern and southwestern Tibet during the Indo-Asian collision. Geological Society of America Bulletin. 111(11), 1644–1664. https://doi.org/10.1130/0016-7606(1999)111<1644:TDHOSA>2.3.CO;2.